

Fine-Tuning and Training of DenseNet for Histopathology Image Representation Using TCGA Diagnostic Slides

Abtin Riasatian¹, Morteza Babaie¹, Danial Maleki¹, Shivam Kalra¹, Mojtaba Valipour², Sobhan Hemati¹, Manit Zaveri¹, Amir Safarpoor¹, Sobhan Shafiei¹, Mehdi Afshari¹, Maral Rasoolijaber¹, Milad Sikaroudi¹, Mohd Adnan¹, Sultaan Shah³, Charles Choi³, Savvas Damaskinos³, Clinton JV Campbell⁴, Phedias Diamandis⁵, Liron Pantanowitz⁶, Hany Kashani¹, Ali Ghodsi^{2,7}, and H.R. Tizhoosh^{1,7}

¹Kimia Lab, University of Waterloo, 200 University Ave. W., Waterloo, ON, Canada

²School of Computer Science, University of Waterloo, 200 University Ave. W., Waterloo, ON, Canada

³Huron Digital Pathology, 1620 King Street North, St. Jacobs, ON, Canada

⁴Department of Pathology and Molecular Medicine, McMaster University, Hamilton, Canada

⁵Laboratory Medicine and Pathobiology, University of Toronto, ON, Canada

⁶Department of Pathology, University of Pittsburgh Medical Center, PA, USA

⁷Vector Institute, 661 University Ave Suite 710, Toronto, ON, Canada

Abstract—Feature vectors provided by pre-trained deep artificial neural networks have become a dominant source for image representation in recent literature. Their contribution to the performance of image analysis can be improved through fine-tuning. As an ultimate solution, one might even train a deep network from scratch with the domain-relevant images, a highly desirable option which is generally impeded in pathology by lack of labeled images and the computational expense. In this study, we propose a new network, namely *KimiaNet*, that employs the topology of the DenseNet with four dense blocks, fine-tuned and trained with histopathology images in different configurations. We used more than 240,000 image patches with 1000×1000 pixels acquired at $20\times$ magnification through our proposed “high-cellularity mosaic” approach to enable the usage of weak labels of 7,126 whole slide images of formalin-fixed paraffin-embedded human pathology samples publicly available through the The Cancer Genome Atlas (TCGA) repository. We tested KimiaNet using three public datasets, namely TCGA, endometrial cancer images, and colorectal cancer images by evaluating the performance of search and classification when corresponding features of different networks are used for image representation. As well, we designed and trained multiple convolutional batch-normalized ReLU (CBR) networks. The results show that KimiaNet provides superior results compared to the original DenseNet and smaller CBR networks when used as feature extractor to represent histopathology images.

Index Terms—Histopathology, Deep Learning, Transfer Learning, Image Search, Image Classification, Deep Features, Image Representation, TCGA

I. INTRODUCTION

Conventional light microscopy is a well-established technology with centuries of history. The adoption of digital pathology that replaces the microscope with a digital scanner

and computer monitor has gained momentum in recent years. The process of digitization of whole slide images (WSIs) offers many advantages such as more efficient workflows, easier collaboration and telepathology, and new biological insights into histopathology data through usage of image processing and computer vision algorithms to detect relevant clinicopathologic patterns (Gurcan et al., 2009; Tizhoosh and Pantanowitz, 2018).

The recent progress in machine learning, particularly deep learning, provides a major argument for proponents of modern pathology to justify the benefits of going digital. Pre-trained, fine-tuned and de novo trained deep networks are being proposed for diverse classification, prediction and retrieval tasks. However, processing WSIs, with or without machine learning, has its own challenges (Madabhushi, 2009). WSIs of histopathology are large files containing complex histologic patterns. Hence, compact and expressive image representation, which is fundamental to image analysis in pathology presents many challenges. Handcrafted features, i.e., image descriptors that have been manually designed based on general image processing knowledge, have been in use as a solution for several decades (Jegou et al., 2011). Many studies, however, have shown that deep features, i.e., high-level embeddings in a properly trained deep network, can outperform handcrafted features in most applications (Kumar et al., 2017). As a result, many different convolutional architectures have been trained and introduced to provide features either directly or through transfer learning (Shin et al., 2016; Mormont et al., 2018). This has created new questions in computer vision research, and consequently in medical image analysis as to which network topology is most suitable for a given task. Is transfer learning sufficient to solve specific problems? What challenges and benefits does training an entire network from scratch entail? (Niazi et al., 2019; Yu et al., 2016; Burt et al., 2018).

In this work, we focus on one of the most successful convolutional topologies in the literature, namely the DenseNet (Huang et al., 2017; Zhang et al., 2019a,b). We fine-tuned and trained the DenseNet architecture with a large number of histopathology patches at 20 times magnification ($20\times$) and compare its search and classification performance, as a feature extractor, against the original DenseNet trained with 1.2 million natural images from ImageNet (Deng et al., 2009). While it is generally expected that fine-tuning and training should deliver more accurate results than transfer learning, the data and experimental challenges inherent in this may easily prevent the expected effects (Glorot and Bengio, 2010; Najafabadi et al., 2015; Srivastava et al., 2015).

In the following sections, we briefly review the relevant literature. We describe how we fine-tuned and re-trained a network, using a large public dataset, which we have named KimiaNet. We report the results of applying KimiaNet on three public datasets for search and classification. We provide details of all experiments to demonstrate the superiority of the KimiaNet features over the original DenseNet features. As well, we report the details of four smaller networks that we designed and trained for bench-marking against KimiaNet.

II. LITERATURE REVIEW

The literature on the applications of deep learning in digital pathology is diverse and contains a multitude of approaches (Janowczyk and Madabhushi, 2016; Niazi et al., 2019; Campanella et al., 2019). As we are focused on image representation, in this section we only review recent works that have used, fine-tuned or trained deep networks for different purposes in digital pathology (Janowczyk and Madabhushi, 2016).

Pre-Trained Networks – Two early examples of off-the-shelf feature extractors are Overfeat (Sharif Razavian et al., 2014) and DeCaf (Donahue et al., 2014) used successfully in breast cancer classification by capturing and combining different fully connected (FC) layers (Spanhol et al., 2017). Combining Inception (V3) features (extracted from multi-magnification pathology images) with a fully connected layer has been used for binary classification in breast cancer metastasis analysis (Liu et al., 2017).

Feature selection from pre-trained deep networks has also been performed in many pathology tasks like HEp-2 protein classification (Phan et al., 2016). Using features from pre-trained networks on pathology domains is another way to classify the pathology problems (Mormont et al., 2018). For instance, features from DeepLoc (Almagro Armenteros et al., 2017) have been used to classify protein subcellular localization (Kraus et al., 2017). As well, deep features from pre-trained networks have been successfully used for image search (Kalra et al., 2019a,b).

Fine-Tuned Networks – It is generally expected that fine-tuning should increase the accuracy of a pre-trained network or the expressiveness of its features in pathology image classification (Kieffer et al., 2017). Faust et al. (2018) fine-tuned the last 2 convolutional blocks of a VGG-19 model initialized with ImageNet weights. More specifically, they utilized annotated patches of size 1024 by 1024 at $20\times$ magnification

from a neuropathology dataset with 13 distinct classes for transfer learning. Eventually, they reported a 95% accuracy for the classification task. Faust et al. (2019) also fine-tuned a VGG-19 model utilizing an extended version of the latter dataset with 74 distinct classes annotated employing the World Health Organization (WHO) tumour classification scheme. Ultimately, they reported the training validation accuracy of 66% over the images spanning the 74 trained classes.

Trained Networks – Coudray et al. (2018) trained an Inception V3 model on 1,176 lung WSIs from the TCGA dataset. They extracted patches of size 512×512 pixels from Lung Adenocarcinoma (LUAD), Lung Squamous Cell Carcinoma (LUSC), and healthy lung tissue slides. Subsequently, they predicted diagnosis associated with any given WSI by assessing the majority vote among the patch level predictions of all tiles of the same slide. Finally, they reported around 97% accuracy for both $20\times$ and $5\times$ magnifications.

Fu et al. (2019) employed transfer learning on 17,396 fresh-frozen tissue images from the TCGA dataset. Their dataset contained 42 classes, including 28 tumour types and 14 healthy tissues. As they removed the non-informative tiles with minimal gradient magnitude, they fine-tuned an Inception V4 utilizing 6.5 million patches of size 512×512 pixels at $20\times$ magnification extracted from the training set WSIs. In the end, they evaluated the power of the learned visual representation by investigating the connection between the WSIs and genome information.

Wei et al. (2019) trained a ResNet architecture using five pathological and benign patterns of lung parenchyma, annotated by three pathologists. They also reported a high level of agreement between their model outcome and the pathologists final diagnosis.

Campanella et al. (2019) suggested a framework based on multiple instance learning and deep neural networks to evaluate WSI-level diagnosis to avoid time-consuming and expensive annotations. First, they trained several ResNet models on different subsets of a dataset made of 44,732 private slides to learn visual representation at both $20\times$ and $5\times$ magnifications. The dataset included prostate cancer, basal cell carcinoma, and metastatic breast cancer involving the lymph nodes. Next, they chose a subset of most the suspicious tiles from each WSI to pass it through a Recurrent Neural Network (RNN) to predict the WSI-level prediction. Bilaloglu et al. (2019) trained a deep convolutional neural network called PathCNN on a dataset comprised of lung cancer, kidney cancer, breast cancer, and non-neoplastic tissues from the TCGA repository. In particular, they extracted regions of size 512×512 pixels at $20\times$ magnification and then downsampled them to 299×299 pixel patches. Similar to previous studies, they predicted WSI-level diagnosis based on the aggregation of the patch-level prediction.

There are a multitude of other possible approaches to customizing deep solution for histopathology images. Multi-instance learning (Campanella et al., 2019), teacher-student learning (Watanabe et al., 2017), and visual dictionaries (Zhu et al., 2018) are among most investigated, to mention a few. Here, we are mainly focused on training and fine-tuning of most commonly used deep topologies.

As the literature shows, we still need to investigate the effect of fine-tuning and training from scratch on expected performance improvement specially using deep embeddings as image features for various tasks. This should ideally be performed using a large public dataset with raw heterogeneous cases not particularly curated for training, hence easily repeatable on many other repositories. As well, images should be processed at high magnification (e.g., $20\times$ or higher) and large enough patches (e.g., $500 \times 500\mu\text{m}^2 \sim 1000 \times 1000$ pixels) to model and cover the workflow for most diagnostic cases. We will investigate the fine-tuning and training of such a network and test its features for search and classification using three public datasets.

Although proposing new architectures and learning algorithms have been the main vehicle of progress within the AI community in recent years, customizing existing topologies is absolutely necessary and may still not be easily possible due to both data and computational challenges. The TCGA repository, for instance, is large and publicly available. However, due to the absence of pixel-level and regional labels of gigapixel files, it is not readily available for training deep networks. Solving practical challenges like this to exploit the discriminative power of deep networks appear to also be a valuable way of knowledge creation. The contribution of the proposed high-cellularity mosaic as whole-slide image representation is enabling the usage of the unlabelled image data by providing an implicit regional annotation, i.e., the mosaic patches of high-cellularity.

Our main contribution is to propose a specialized patch selection method to create a high-cellularity collection – called *cellMosaic* – to enable the usage of weak WSI-level labels of a public multi-organ cancer image archive at high magnification with high-resolution patches with no downsampling for training of a densely connected network. The proposed KimiaNet can then be employed for feature extraction in histopathology.

III. KIMIANET - DATA AND TRAINING

We name our network “*KimiaNet*”¹ as we are convinced that the actual information hidden in big image data can only be extracted through extensive fine-tuning, or better, training from scratch. As there have been extensive research on network topologies, we have chosen a dependable network, called *DenseNet*, as the basis for our investigations.

Customizing well-established architectures for specific and sensitive tasks not only appear to be justified but also seem to be necessary for the sake of application-oriented categorization and end-user awareness. One example is certainly the “CheXNet” that is a fine-tuned DenseNet using x-ray images (Rajpurkar *et al.*, 2017).

Based on the observation that convolutional networks can be very deep, yet more accurate, and still efficient to train “if they contain shorter connections between layers close to the input and those close to the output”, Gao Huang and

his colleagues introduced the densely connected convolutional networks (Huang *et al.*, 2017). The network consists of several dense blocks with preceding convolutional and pooling layer (Figure 1). Most recent works refer to DenseNet topology as a reliable candidate solution for image representation in histopathology (Campanella *et al.*, 2019). Beside the popularity of DenseNet (Lee *et al.*, 2017; Liu *et al.*, 2018), we have already experimented with its features in our previous works (Babaie and Tizhoosh, 2019; Kalra *et al.*, 2019a,b). In addition, compared to the top-10 matching evaluation of networks for bench-marking through ImageNet, DenseNet is certainly a compact architecture with a smaller footprint; the size of DenseNet-121 topology with almost 7M parameters amounts to almost 10% of EfficientNet-B7 (66M parameters) and 0.8% of FixResNeXt-101 32×48d (829M parameters)².

A. Public Image Datasets

It is paramount to use public data such that results are reproducible by other researchers. We downloaded and used three public image datasets: pan-cancer images from The Cancer Genome Atlas (TCGA) repository ($\approx 33,000$ WSIs for 32 primary diagnosis), endometrial cancer images ($\approx 3,300$ patches from 4 classes), and colorectal cancer images (5,000 patches from 8 classes). Whereas TCGA provides WSIs with primary diagnosis for the entire image, both colorectal and endometrial datasets contain labelled patches. We used most TCGA images for training and some for testing; both colorectal and endometrial datasets were exclusively used for testing.

1) *TCGA Images*: The TCGA repository (i.e., Genomic Data Commons, GDC³) with 30,072 WSIs is a publicly available repository (Gutman *et al.*, 2013; Tomczak *et al.*, 2015; Cooper *et al.*, 2018). We recorded 29,120 WSI fully readable files at $20\times$ magnification (approximately 6 terabytes in compressed form) to prepare the dataset for training. Although $40\times$ magnification images were also available in many cases, we did use $20\times$ magnification to maximize the size of the dataset. The dataset contains 25 anatomic sites with 32 cancer subtypes. Brain, endocrine, gastrointestinal tract, gynecological, hematopoietic, liver/pancreaticobiliary, melanocytic, prostate/testis, pulmonary, and urinary tract had more than one primary diagnoses such that they could be used for subtype classification. From the 29,120 WSIs, 26,564 specimens were neoplasms, and 2,556 were non-neoplastic. A total of 17,425 files comprised of frozen section digital slides were removed from the dataset due to their lower quality. We did not use frozen sections because the freezing artefacts in these images can “confound routine pathological examination or image analysis algorithms” (Cooper *et al.*, 2018). We kept 11,579 of permanent hematoxylin and eosin (H&E) sections for training and testing. We did not remove manual pen markings from the slides when present. This pre-selection of TCGA images will be further refined to assemble the training, validation and testing datasets (see Section III-C).

¹The Persian/Arabic word *kīmiyā* and its Greek version *khēmeia* appear to originate from the Coptic word *kēme* (meaning *Egypt*) and is believed to be the root word for “chemistry” and associated with the *alchemy* that tried to purify metals and convert them to gold.

²<https://sotabench.com/benchmarks/image-classification-on-imagenet>

³<https://portal.gdc.cancer.gov/>

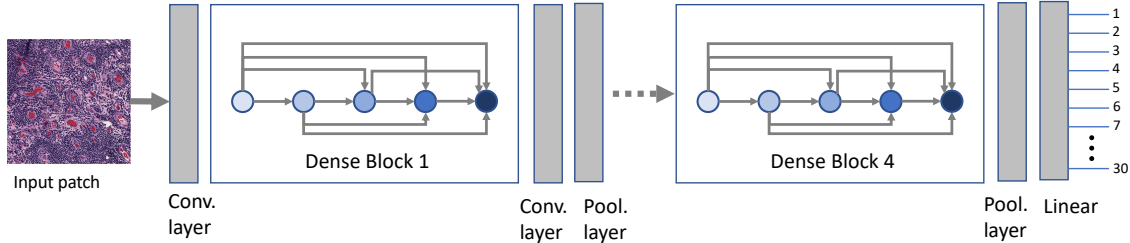


Fig. 1. DenseNet architecture of KimiaNet.

TABLE I
ENDOMETRIUM DATASET (SUN ET AL., 2019)

Class	Number of patches
Normal Endometrium (NE)	1,333
Endometrial Polyp (EP)	636
Endometrial Hyperplasia (EH)	798
Endometrial Adenocarcinoma (EA)	535

2) *Endometrium dataset*: Recently the endometrium dataset was introduced to compare a deep learning method (HIENet) classification ability versus four experienced pathologists (Sun et al., 2019). In this dataset, there are four classes of endometrial tissue, namely normal, endometrial polyp, endometrial hyperplasia, and endometrial adenocarcinoma. Table I shows the class distribution of all 3,302 images in the endometrium dataset. Patches of size 640×480 pixels are extracted from $20\times$ or $10\times$ magnification WSIs and saved as JPEG files⁴. Although all slides have been prepared and scanned at the same hospital, considerable stain variation can be observed across endometrium patches.

3) *Colorectal Cancer Dataset*: One of the first digital pathology classification datasets, the colorectal cancer images (Kather et al., 2016), consists of 5,000 samples in 8 classes and 625 small patches (150×150 pixels) in each class. Labels in this dataset are tumour epithelium, simple stroma, complex stroma, immune cells, debris, normal mucosal glands, adipose tissue and background patches.

Figure 2 shows sample images for each of the three datasets.

B. Processing Unlabelled Big WSI Data

Due to the large size of digital pathology images, representing WSI files is still an obstacle for many tasks in computational pathology (Tizhoosh and Pantanowitz, 2018). Most approaches therefore focus on patch processing. The TCGA data only provides WSIs such that patches have to be extracted. As well, images are not labelled in the common sense. That means there is no manual delineation of regions of interest (i.e., malignant pixels); TCGA WSIs are associated with a primary diagnosis for the entire image which may also contain healthy tissue. This makes the creation of a dataset of patches somewhat difficult as we need to feed labelled patches (i.e., small sub-images) into a deep network.

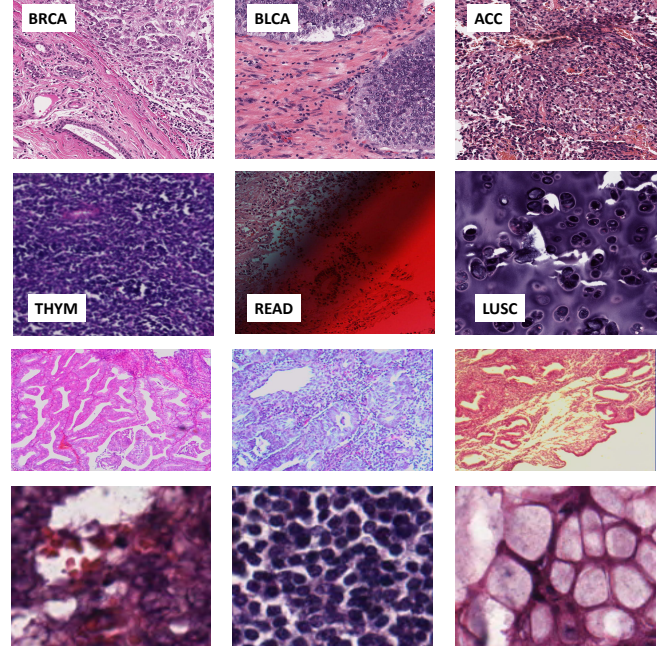


Fig. 2. Sample patches from the three datasets: TCGA repository (top two rows with the 1st row for good quality and 2nd row for low quality samples), endometrial cancer (3rd row), and colorectal cancer (bottom row).

Yottixel is a recently proposed image search engine for histopathology (Kalra et al., 2019a,b). We used a modified Yottixel indexing followed by post-processing to extract labelled patches from TCGA dataset (see Algorithm 1). Yottixel assembles a “mosaic” of each WSI at magnification m_I through patching and clustering at magnification m_C with patches at size $l \times l$ grouped in n_C clusters. The mosaic is a rather small collection of patches, i.e., p percentage of the image area, at magnification m_I to represent the entire WSI. Here, the main difference with the original Yottixel mosaic is the function *cellMosaic* (line 13, Algorithm 1) that modifies the mosaic M into a new mosaic M' by removing all patches with low cellularity by taking the top T_{Cell} percent of cellularity-sorted patches. Based on the assumption that many high-grade carcinomas may have higher cellularity levels compared with healthy tissue, M' enables us to use the WSI label (i.e., the primary diagnosis) for all remaining patches of each WSI, hence making the TCGA data usable for training a network.

⁴Download: <https://doi.org/10.6084/m9.figshare.7306361.v2>

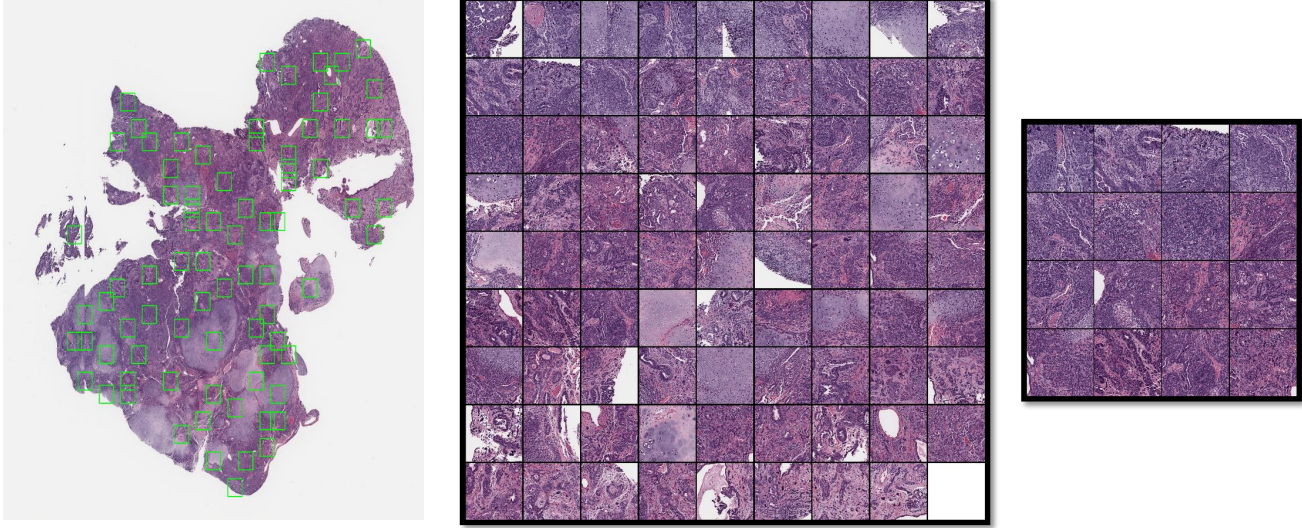


Fig. 3. A WSI and its selected mosaic patches (left), Yottixel mosaic with 80 patches (middle), modified *cellMosaic* with 16 patches (right).

Algorithm 1 Modified Yottixel Algorithm

```

1:  $m_I \leftarrow 20x$                                 ▷ Magnification for indexing
2:  $m_C \leftarrow 5x$                                 ▷ Magnification for clustering
3:  $l \leftarrow 1000$                                 ▷ Patch size  $l \times l$  at  $m_I$ 
4:  $n_C \leftarrow 9$                                 ▷ Number of clusters at  $m_C$ 
5:  $p \leftarrow 15\%$                                 ▷ Mosaic percentage
6:  $T_{Cell} \leftarrow 20\%$                                 ▷ Top cases among sorted cellularity
7:  $\mathbf{A} \leftarrow \text{readWSI}(fileName)$                 ▷ Read an image
8: procedure YOTTIXELINDEX( $\mathbf{A}, m_I, m_C, l, n_C, p, T_{Cell}$ )
9:    $\mathbf{S} \leftarrow \text{Segment}(\mathbf{A}, m_C)$  ▷ Separate tissue/background
10:   $P \leftarrow \text{Patching}(\mathbf{A}, \mathbf{S}, m_I, l)$           ▷ Get all patches
11:   $C \leftarrow \text{KMeansCluster}(P)$                   ▷ Cluster patches
12:   $M \leftarrow \text{getMosaic}(C, p, \mathbf{A})$             ▷ Select a mosaic
13:   $M' \leftarrow \text{cellMosaic}(M, T_{Cell})$         ▷ Keep cell patches
14:   $F \leftarrow \text{Network}(M')$                       ▷ Get features
15: return  $F$                                     ▷ Set of features for  $\mathbf{A}$ 

```

C. Training Data

To create the dataset, we first eliminated frozen sections so that only permanent section diagnostic slides were left. The low quality of frozen section images might negatively affect training. In order to create a versatile dataset, we divided the data into groups with most detailed labels, each unique group being specified by combination of ‘morphology’, ‘primary diagnosis’ and ‘tissue or organ of origin’ label. Then, we removed the groups with fewer than 20 cases so the dataset can be used at the most detailed level by specifying the label of each class with the mentioned combination; hence, each class has at least 2 cases (ten percent of 20) test samples. For example, one of the deleted groups was [‘8020/3’, ‘Carcinoma, undifferentiated, NOS’, ‘Tail of pancreas’] which had only one case. As a result of this process, 2 of the 32 classes of primary diagnoses were removed, the UCEC (Uterine Corpus Endometrial Carcinoma) class due to the morphology

information not being reported at the time of creating the dataset and the DLBC (Lymphoid Neoplasm Diffuse Large B-cell Lymphoma) class for not having any detailed groups with at least 20 cases. We used tumour type categorization based on established literature (Cooper *et al.*, 2018). For instance, LUAD (lung adenocarcinoma), LUSC (lung squamous cell carcinoma) and MESO (mesothelioma) would all fall under “Pulmonary Tumours”. This is particularly useful for evaluation of horizontal search. The test and validation datasets were chosen from the single cases randomly selecting from 10% of WSIs within each class. The rest of the slides were assigned to the training dataset. All cases that did not contain diagnostic or morphological information were removed from all datasets. This resulted into a test dataset of 777 slides, a validation dataset of 776 slides and training dataset of 7,375 diagnostic slides. All three sets are disjoint. In Particular, we selected both test and validation sets to only consist of those patients with only one diagnostic slide. As well, WSIs with no magnification information or with magnification lower than 20 \times were removed. This led to creation of a test dataset of 744 slides, a validation dataset of 741 slides and a training dataset of 7,126 slides (**a total of 8,611 WSIs**). Extracting 500 μ \times 500 μ at 20 \times finally resulted in 1,198,118 patches for training, 121,801 patches for validation, and 116,088 patches for testing.

Pathologists generally use different patch sizes and samples to find different types of information. For instance, 10 \times is used for gross features and infiltrates, 20 \times for more detailed histology patterns, and 40 \times for fine nuclear and cellular details. Both magnification level and patch size are set based on empirical evidence and computational convenience (some works have used similar settings as in this work, e.g., see Faust *et al.* (2018)). The algorithms proposed in this work can be run for any magnification and any patch size if desired histologic features are apparent and/or computational resources available.

The dataset was still not suitable for training; as the WSIs were labeled with diagnosis, and not the patches. However, we intended to train the network at the patch level. The patch dataset included multiple healthy/benign patches associated with a diseased WSI. This would perhaps confuse any deep network during training. As carcinomas are generally associated with uncontrolled cell growth, mainly embodied in areas with unusually high presence of cell nuclei (e.g., small cell carcinoma is extremely hypercellular), cellularity of patches can be used to eliminate most benign/healthy patches (Travis, 2014)⁵. We chose hypercellularity to automate patch selection as this is one of the principal hallmark features of cancer that spans most neoplasms. Cellularity can be used as an initial filter to select patches with a higher probability of malignancy. However, we realize that reactive or inflammatory tissue features may in some cases also be included in this set. While we do recognize that non-neoplastic cell types may show hypercellular regions, we feel these caveats are outweighed by the superior automation provided by this approach. Similar approaches have been used recently when patches with minimal gradient magnitudes were eliminated (Fu *et al.*, 2019). Hence, we measured the *cellularity* of each patch. This was done by first deconvolving the patch color from RGB to hematoxylin and eosin channels using color deconvolution (Onder *et al.*, 2014)⁶. Then a binary mask was created from the hematoxylin channel using a constant threshold, set empirically, to get the cellularity ratio for each patch (Figure 4). Finally, training and validation dataset patches were each sorted with respect to their ratio of cellularity (number of pixels with value 1 in the created mask over the number of all patch pixels). The top $T_{Cell} = 20\%$ patches (lines 6 and 13, Algorithm1) with regard to their sorted ratio were selected with the additional constraint of having a file size larger than a specific threshold (e.g., >100 KB). This resulted into final training and validation datasets containing **242,202** and **24,646** patches, from **7,126 and 741** WSIs, respectively. Hence, we are using a 80%-10%-10% split for training/validation/testing to assign as many samples as possible to the training data. Besides, the restrictions on testing data geared the ratio also toward larger this split.

D. Training

We run the training/fine-tuning in several configurations to generate KimiaNet-I (last DenseNet-121 block trained), KimiaNet-II (last two DenseNet-121 blocks trained), KimiaNet-III (last three DenseNet-121 blocks trained), and KimiaNet-IV (all DenseNet-121 blocks trained).

We used the *PyTorch* platform to train and test the models described above. We trained each model on 4 Tesla V100 GPUs with 32GB memory per GPU. We set the batch size of

⁵Although abnormal and disrupted tissue architecture is another major criterion to select candidate patches, this may be more challenging to accomplish compared to cellularity measurements.

⁶We used the function available in HistomicsTK library on GitHub: The RGB image is transformed into optical density space, and then projected onto the stain vectors in the columns of the stain matrix W , a 3×3 matrix containing the color vectors in columns. For two stain images the third column is zero and will be complemented using cross-product. For deconvolving H&E stained image, W is set to $[[0.650, 0.072, 0], [0.704, 0.990, 0], [0.286, 0.105, 0]]$.

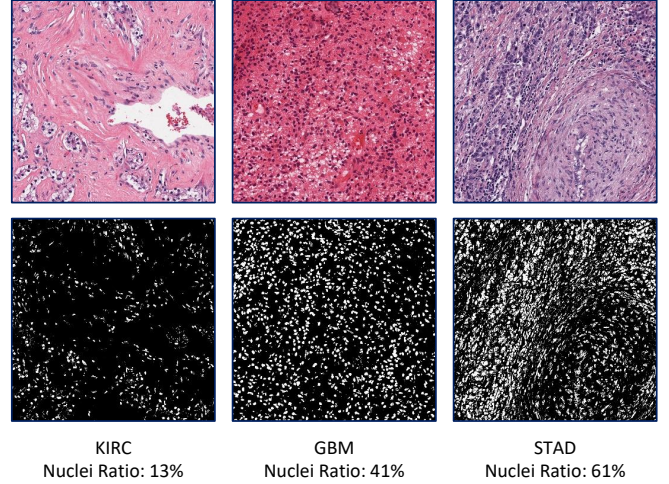


Fig. 4. Samples for cell segmentation.

256, 128, 128 and 64 for KimiaNet-I, KimiaNet-II, KimiaNet-III and KimiaNet-IV, respectively. Each network was trained for roughly 20 epochs. Each epoch took approximately 60, 75, 90 and 110 minutes for KimiaNet configurations I, II, III and IV, respectively. We used 30 classes of primary diagnoses as the KimiaNet output (see Table VI in Appendix). The stopping criterion for training is a decrease in validation accuracy for three consecutive epochs. We used the Adam optimizer (Kingma and Ba, 2014) for optimization of our models with an initial learning rate of 0.0001 and scheduler that decreases the learning rate every 5 epochs. We set the cross-entropy as the loss function for our models to measure the performance of the classification model. For each of the models, we used the ImageNet pre-trained weights for initialization. One has to bear in mind that the DenseNet has been trained with 1.2 million images for 1,000 classes; KimiaNet has been trained with 242,202 images (data ratio = $242,202/1,200,000 \approx 0.20$) for 30 classes (class ratio = $30/1,000 = .03$).

Figure 5 shows the convergence behaviour of all four models. In most experiments, convergence was observable after 10 epochs. Clearly, the highest accuracy values were achieved when we trained KimiaNet-IV by re-training all DenseNet-121 weights. The general trend of getting higher accuracy by fine-tuning more blocks is also visible.

IV. EXPERIMENTS

Once the training of different versions of KimiaNet were completed, we used the three datasets to measure the generalization capability of KimiaNet's features extracted from its last pooling layer. The DenseNet features from the same layer were extracted as well for comparison. When searching through features/barcodes to find matches, we used k -NN algorithm (with $k = 3$) to find the top k matched (most similar) features/barcodes. The top k matched images through search can be retrieved along with their corresponding metadata. However, we treat the search like a classifier to quantify its performance.

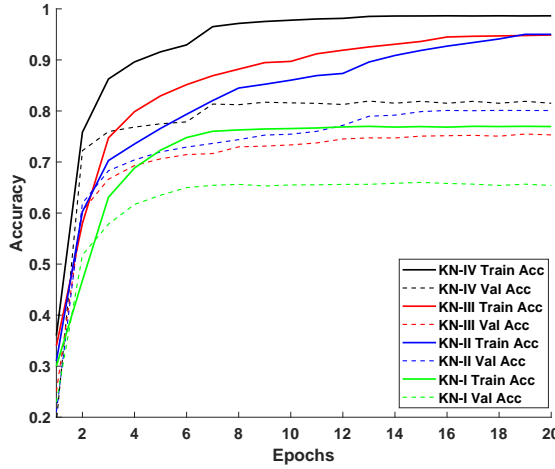


Fig. 5. Training/validation accuracy for different KimiaNet configurations.

So far, we have mentioned major parameters for KimiaNet. Clearly, any solution based deep networks has many parameters and hyperparameters that need to be adjusted (Cui and Bai, 2019). In the case of histopathology gigapixel images, additional parameters may be added for operation such as segmentation, patching and clustering (Kalra *et al.*, 2019a).

A. TCGA Experiments: Classification through Search

To evaluate the distinctive power of the provided features, two types of experiments were performed on the testing images: 1) *Horizontal search* which means measuring how accurate the algorithm can find the tumour type across the entire test dataset, and 2) *Vertical search* which is defined as finding the right primary diagnosis of a tumour type among the slides of a specific primary site (containing different primary diagnoses). The features were “barcoded” for faster search (Tizhoosh *et al.*, 2016; Kalra *et al.*, 2019a). Barcoding refers to binarization of deep features based on their point-to-point changes (increase/decrease is encoded as 1/0; $a-b$ is 1 whereas $b-a$ is 0 when $a < b$). Not only binary operations are much faster than arithmetic operations on real-valued features, but also we have already observed that encoding the gradient of deep feature may even increase the matching accuracy (Kumar *et al.*, 2018).

We used the k -nearest neighbors algorithm (k -NN) approach with Hamming distance to compare the barcoded features of individual patches. For horizontal search the classification accuracy was used whereas for vertical search we calculated the F1 scores. The results for horizontal search are reported in Table II and Figure 6.

Analysis of Horizontal Search – As Table II shows KimiaNet improves the search accuracy in all cases (on average $41\% \pm 14\%$). A Kolmogorov-Smirnov test of normality delivered a test statistic of $D = 0.25079$ for DenseNet ($p = 0.27417$) and $D = 0.28253$ for KimiaNet IV ($p = 0.2433$). Hence, both distributions did not differ significantly from a normal distribution. DN showed an average accuracy

TABLE II

3-NEAREST NEIGHBORS ACCURACY (%) FOR THE HORIZONTAL SEARCH AMONG 744 WSIS FOR DIFFERENTLY FINE-TUNED/TRAINED KIMIANET. THE BEST RESULTS ARE HIGHLIGHTED. THE LAST COLUMN SHOWS THE IMPROVEMENT OF ACCURACY (%) THROUGH KIMIANET COMPARED TO DENSENET.

Tumor Type	Patient #	DN	I	II	III	IV	diff
Brain	74	72	96	97	99	99	+27
Breast	91	53	86	87	91	91	+38
Endocrine	72	65	86	89	93	92	+28
Gastro.	88	53	74	81	80	84	+31
Gynaec.	30	13	43	40	47	57	+44
Head/neck	32	25	75	69	81	88	+63
Liver	51	43	67	69	80	88	+45
Melanocytic	28	18	57	54	75	86	+68
Mesenchymal	13	23	38	62	69	69	+46
Prostate/testis	53	57	89	91	94	96	+39
Pulmonary	86	56	83	86	85	86	+30
Urinary tract	123	59	89	89	88	89	+30

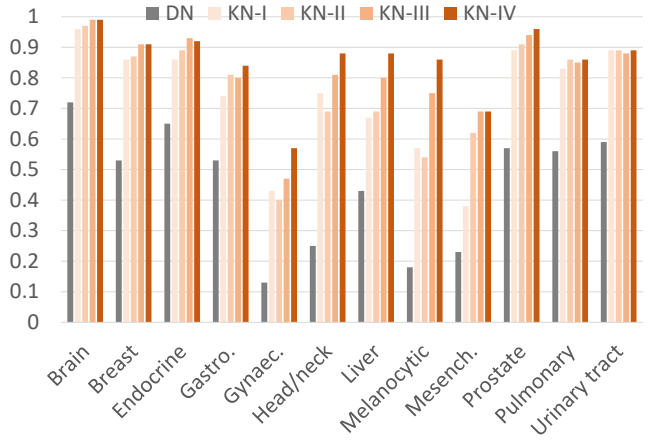


Fig. 6. Horizontal search results (accuracy, in percentage) for TCGA data.

of 44.8% ($\text{std}=19.9\%$) whereas KN-IV delivered an average accuracy of 85.4% ($\text{std}=11.6\%$). With 68% improvement, melanocytic malignancies benefited the most from KimiaNet features. However, the performance for head and neck (63%) and mesenchymal (54%) has also shown substantial increase over the average improvement. Although brain has the lowest improvement (27%), its search accuracy reaches 99% with KimiaNet compared to 72% with DenseNet.

For cancer subtyping, we run the vertical search where we confined the search to each tumour site to extract the correct diagnosis for each primary site. WSIs were recognized through the “median-of-min” approach: the minimum Hamming distance for each patch of the query mosaic was calculated when compared to all patches of other WSIs. The median value of all minimum distances was taken as the matching score for the query WSI. Figure 7 shows sample queries and results for both DenseNet and KimiaNet. Examination of t-SNE visualization, applied on test images, showed that KimiaNet features have superior class discrimination (Figure 8). Detailed results are reported in Table III. Here, we used the F1-measure to account for sensitivity and specificity.

Analysis of Vertical Search – The higher discrimination power of KimiaNet features is clear. This is not only mani-

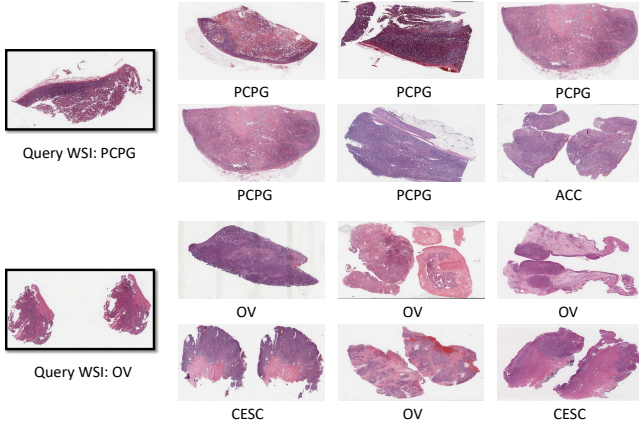


Fig. 7. Results for two sample query WSIs (left): Corresponding search results based on KimiaNet features (top row for each query WSI) and DenseNet features (bottom row for each query WSI) and their assigned TCGA primary diagnosis. For TCGA project IDs see Table VI in Appendix.

TABLE III

k-NN RESULTS FOR THE VERTICAL SEARCH AMONG 744 WSIS. THE BEST RESULTS ARE HIGHLIGHTED. F1-MEASURE HAS BEEN REPORTED HERE INSTEAD OF SIMPLE CLASSIFICATION ACCURACY. FOR TCGA CODES SEE TABLE VI IN APPENDIX.

Site	Subtype	<i>n</i> slides	DN	I	II	III	IV
Brain	LGG	39	71	75	82	85	81
Brain	GBM	35	77	73	80	83	81
Endocrine	THCA	51	94	98	98	99	100
Endocrine	ACC	6	25	25	20	55	44
Endocrine	PCPG	15	57	75	73	80	85
Gastro.	ESCA	14	50	73	50	83	78
Gastro.	COAD	32	65	76	75	75	76
Gastro.	STAD	30	63	77	73	84	86
Gastro.	READ	12	22	30	26	29	30
Gynaeco.	UCS	3	75	86	60	75	86
Gynaeco.	CESC	17	88	97	84	97	94
Gynaeco.	OV	10	67	89	74	95	95
Liver, panc.	CHOL	4	29	40	31	40	40
Liver, panc.	LIHC	35	86	94	87	97	96
Liver, panc.	PAAD	12	70	73	56	82	76
Melanocytic	SKCM	24	92	94	94	98	94
Melanocytic	UVM	4	0	40	40	86	67
Prostate/testis	PRAD	40	99	100	99	100	100
Prostate/testis	TGCT	13	96	100	96	100	100
Pulmonary	LUAD	38	65	73	72	69	78
Pulmonary	LUSC	43	69	74	74	75	84
Pulmonary	MESO	5	0	0	0	33	75
Urinary tract	BLCA	34	90	96	93	93	93
Urinary tract	KIRC	50	83	95	99	97	97
Urinary tract	KIRP	28	77	91	91	91	91
Urinary tract	KICH	11	48	86	78	84	86

fested in the t-SNE visualization (Figure 8) but also quantified in F1-measures (Table III). For all subtypes, the F1 score of KimiaNet is higher than DenseNet.

B. Endometrium Data Experiments: Classification

To verify the performance of deep features of KimiaNet on the pathology datasets in comparison with other networks, we conducted several experiments on Endometrium images as one of the most recently released datasets. One of these experiments is comparing KimiaNet to another histopathology feature extractor, which is a fine-tuned VGG-19 using 838,644 human-annotated histopathologic patches spanning 74 different lesional and non-lesional tissue types (Faust et al., 2019). We extracted deep features from all patches with the

TABLE IV
RESULTS FOR COLORECTAL CANCER DATASET.

Methods	Accuracy
Combined features (Kather et al., 2016)	87.40%
Fine-tuned VGG-19 on 74 classes (Faust et al., 2019)	93.58%
DenseNet	94.90%
KN-I	96.38%
KN-IV	96.80%
Ensemble of CNNs Here1 (Nanni et al., 2018)	97.60%

network input default size (224×224 pixels for DenseNet, 1000×1000 pixels for KimiaNet, and 1024×1024 pixels for the fine-tuned VGG-19). Subsequently, features of each network were used to classify the images using SVM (Support Vector Machines). Ten fold cross-validation with fixed folds, was performed to train the best classifier in each case. The Cubic SVM outperformed all other SVM versions. As Figure 9 demonstrates, with 81.41% KimiaNet features showed improvement surpassing HIEnet with 76.91% and the fine-tuned VGG-19 with 76.38%. Figure 10 illustrates the confusion matrices of DenseNet and KimiaNet.

C. Colorectal Data Experiments: Classification

In the last experiment, we repeated the previous experiments with the colorectal dataset. KimiaNet delivered higher accuracy than DenseNet and the fine-tuned VGG-19 (Table IV) whereas only an ensemble CNN approach provided higher accuracy. The confusion matrix for KimiaNet shows a pronounced diagonal (Figure 11).

D. High-Cellularity Mosaic

The cellMosaic is a novel approach using weak/soft labels on valuable large datasets like the TCGA that are not annotated at the pixel level. Using the cellMosaic has apparently enabled KimiaNet to outperform DenseNet for TCGA diagnostic images. As we envision using KimiaNet as a feature extractor for histopathology (and not as a classifier), the cellMosaic may also have induced a bias toward high-grade carcinomas and perhaps inflammations with high-cellularity. The additional experiments with two other dataset provided confidence that KimiaNet can in fact represent histopathology patterns in a variety of single patches, and not in cellMosaic as for TCGA whole-slide images. For instance, the CRC dataset contains classes like adipose, debris, normal and background with low to no cellularity at all, and KimiaNet features were able to distinguish them from tumour epithelium with high-cellularity. However, more experiments with other datasets would be beneficial to more closely define the KimiaNet's application domain.

E. CBR Nets: Small versus large

According to recently published results, smaller topologies may in fact provide better or the same results for medical images as delivered by large networks pre-trained and tested using datasets like ImageNet (Raghu et al., 2019).

Compact and simple networks made of repetitions of convolutional, batch-normalization and ReLU layers, also called

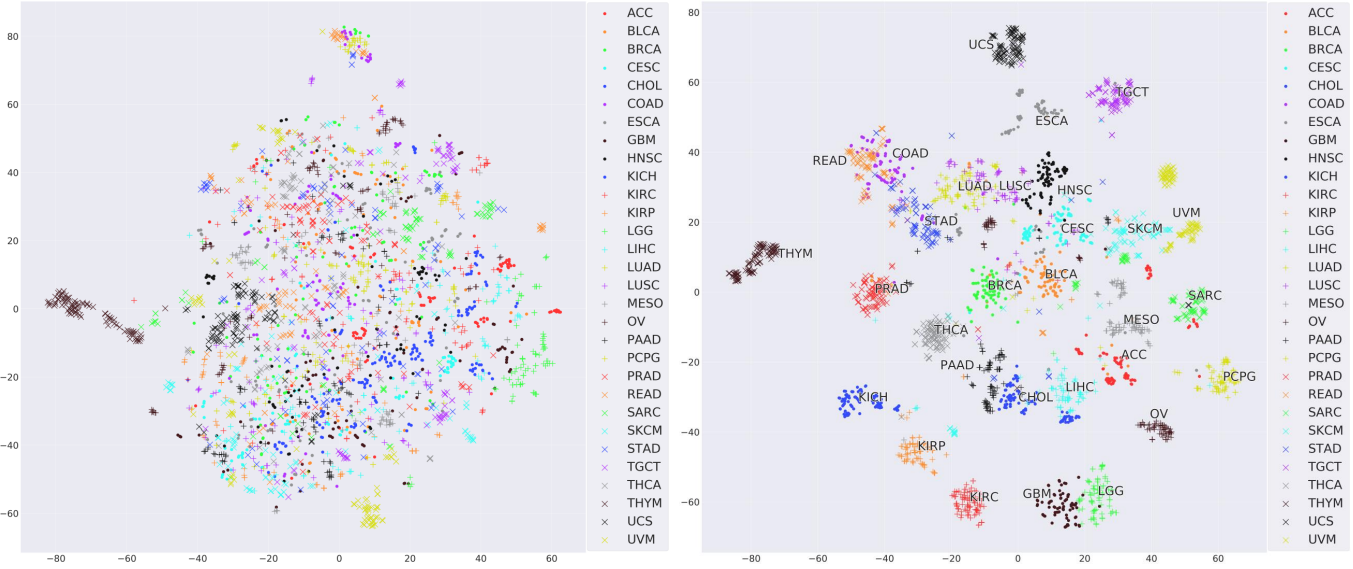


Fig. 8. t-SNE visualization of randomly selected test images for DenseNet (left) and KimiaNet (right).

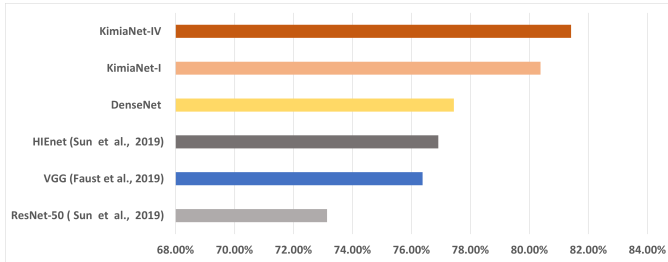


Fig. 9. Endometrium dataset: SVM accuracy for different deep features: Fine-tuned VGG vs. DenseNet vs. HIEnet vs. KimiaNet for different input sizes.

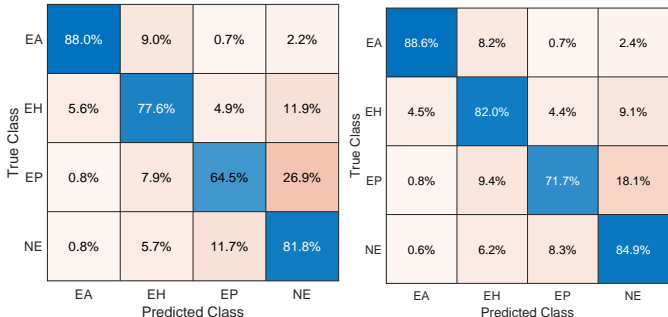


Fig. 10. Confusion matrices for DenseNet (left) and KimiaNet features (right) for the endometrium dataset.

CBR nets, have been found to be quite accurate, compared to larger standard ImageNet models, for applications such as retinal and x-ray image identifications. Raghu *et al.* (2019) investigated large networks like ResNet50 (~23.5M weights) and Inception-V3 (~23M weights) and showed that, for instance, the Small CBR network (~2M weights) generated comparable results. The authors, however, did not investigate the popular DenseNet121 (~7M weights). In order to verify our results in light of these recent experiments, we did implement

	AT	BP	CS	De	IC	NMG	SS	TE
True Class	AT	BP	CS	De	IC	NMG	SS	TE
AT	97.8%	1.8%		0.3%			0.2%	
BP	0.5%	99.5%						
CS			93.4%	0.3%	2.2%	0.6%	2.1%	1.3%
De	1.0%		0.5%	96.5%		1.0%	1.1%	
IC			1.6%		98.1%	0.2%	0.2%	
NMG			0.3%	0.6%	0.8%	97.6%		0.6%
SS			3.0%	1.6%	0.3%	0.2%	94.6%	0.3%
TE			1.3%		0.5%	0.8%	0.5%	97.0%

Fig. 11. CRC dataset confusion matrix for KimiaNet features.

TABLE V
AVERAGE AND STANDARD DEVIATION OF ACHIEVED SCORE (ACCURACY FOR HORIZONTAL AND F1 SCORE FOR VERTICAL SEARCH) FOR EACH TOPOLOGY FOR TCGA IMAGES. n_{MAX} IS NUMBER OF TIMES MAXIMUM SCORE ACHIEVED (OUT OF 12 AND 26 CLASSES FOR HORIZONTAL AND VERTICAL SEARCH RESPECTIVELY) AND $n_{WEIGHTS}$ IS THE APPROXIMATE NUMBER OF PARAMETERS FOR THE TOPOLOGY.

Topology	Horizontal	n_{max}	Vertical	n_{max}	$n_{weights}$
CBR Small	48 ± 20	0	69 ± 24	1	2 Millions
CBR Mod. Small	46 ± 22	0	68 ± 29	1	5.5 Millions
CBR LargeT	55 ± 20	0	69 ± 23	3	8.5 Millions
CBR LargeW	50 ± 22	0	71 ± 24	2	8.5 Millions
DN	45 ± 20	0	64 ± 28	0	7 Millions
KN IV	85 ± 12	12	81 ± 18	23	7 Millions

and test multiple CBR network topologies to validate against KimiaNet.

We implemented the Small, LargeT and LargeW topologies as suggested by Raghu *et al.* (2019) with a slight modification of adding a dense layer before the last fully connected layer⁷.

⁷The performance of CBR features was very low without the additional dense layer.

We also implemented a modified Small network by adding the fifth CBR block to the Small topology. The networks were initialized with random weights and trained from scratch for around 40 epochs using the same TCGA dataset as used for KimiaNet. All settings were the same as for the training of KimiaNet except that the learning rate was initialized with 0.003 and the batch size was 32.

Tables V shows the results of the experiments for horizontal and vertical search. For horizontal search, it can be observed that KimiaNet achieves a considerably higher accuracy average with more consistency than all other networks, having a 30% difference with the second best results (LargeT with around 1.5 M parameters more than KimiaNet). In addition, KimiaNet achieves the maximum accuracy for all of the classes (12 in horizontal search) while none of other networks reached the maximum accuracy for any of the classes. There is a similar pattern for vertical search. The average of F1 scores for KimiaNet is 10% higher than the second best network, LargeW, which, again, has more parameters than KimiaNet. KimiaNet's low standard deviation of F1 scores shows its stability compared to other networks and the number of maximum F1 scores (23 out of 26 classes) confirms its superiority over CBR networks.

V. SUMMARY AND CONCLUSIONS

The question of image representation is generally an important topic in computer vision and becomes critical in digital pathology due to the texture complexity, polymorphism, and the sheer size of WSIs. Examining recent works clearly shows that high-level embeddings in artificial neural networks are considered the most robust and expressive source for image representation. Pre-trained networks such as DenseNet that draw their discrimination power from intensive training with millions of natural (non-medical) images have found widespread usage in medical image analysis. Several attempts have been reported in literature to fine-tune or train deep networks with histopathology images, a desirable task that is impeded by lack of labelled image data and the need for high-performance computing devices.

In this work, we proposed KimiaNet in several fine-tuned configurations by using a clustering-based mosaic structure for image representation modified by relying on high cellularity in order to enable the usage of WSI-level labels in archives with no pixel-level annotations. Three public datasets were employed to generate the results. While there are several approaches to the application of neural networks to medical image analysis, the narrow focus on a single problem/approach within a given study limits guidance on how best to optimize neural networks for pathology tasks.

Our main contribution in this paper was exploiting a diverse, multi-organ public image repository like TCGA at $20\times$ magnification to extract large patches, 1000×1000 pixels at high resolution, for training a densely connected network with weak labels to serve as feature extractor. As well, we showed that fine-tuning a deep network on a sufficiently large number of histopathology images delivers better performance than a pre-trained network model. Finally, we think the publicly

available data and code are valuable for the computational pathology community. The proposed high-cellularity mosaic crucially facilitated the training but may have introduced a bias toward certain histologic features at the expense of visual similarities. Future works have to carve out a comprehensive list of histopathology applications that could benefit from KimiaNet for image representation.

Acknowledgements – The authors would like to thank the Ontario government for the ORF-RE (Ontario Research Fund - Research Excellence) and NSERC (Natural Sciences and Engineering Research Council of Canada) that have funded this research.

Data/Code Availability – KimiaNet and the folds for the validation of all datasets will be available for download from “<https://kimia.uwaterloo.ca>”.

REFERENCES

- Almagro Armenteros, J.J., Sønderby, C.K., Sønderby, S.K., Nielsen, H., Winther, O., 2017. Deeploc: prediction of protein subcellular localization using deep learning. *Bioinformatics* 33, 3387–3395.
- Babaie, M., Tizhoosh, H.R., 2019. Deep features for tissue-fold detection in histopathology images. *arXiv preprint arXiv:1903.07011* .
- Bilaloglu, S., Wu, J., Fierro, E., Sanchez, R.D., Ocampo, P.S., Razavian, N., Coudray, N., Tsirigos, A., 2019. Efficient pan-cancer whole-slide image classification and outlier detection using convolutional neural networks. *bioRxiv* , 633123.
- Burt, J.R., Torosdagli, N., Khosravan, N., RaviPrakash, H., Mortazi, A., Tissavirasingham, F., Hussein, S., Bagci, U., 2018. Deep learning beyond cats and dogs: recent advances in diagnosing breast cancer with deep neural networks. *The British journal of radiology* 91, 20170545.
- Campanella, G., Hanna, M.G., Geneslaw, L., Miraflor, A., Silva, V.W.K., Busam, K.J., Brogi, E., Reuter, V.E., Klimstra, D.S., Fuchs, T.J., 2019. Clinical-grade computational pathology using weakly supervised deep learning on whole slide images. *Nature medicine* 25, 1301–1309.
- Cooper, L.A., Demicco, E.G., Saltz, J.H., Powell, R.T., Rao, A., Lazar, A.J., 2018. Pancancer insights from the cancer genome atlas: the pathologist’s perspective. *The Journal of pathology* 244, 512–524.
- Coudray, N., Ocampo, P.S., Sakellaropoulos, T., Narula, N., Snuderl, M., Fenyö, D., Moreira, A.L., Razavian, N., Tsirigos, A., 2018. Classification and mutation prediction from non-small cell lung cancer histopathology images using deep learning. *Nature medicine* 24, 1559.
- Cui, H., Bai, J., 2019. A new hyperparameters optimization method for convolutional neural networks. *Pattern Recognition Letters* 125, 828–834.
- Deng, J., Dong, W., Socher, R., Li, L.J., Li, K., Fei-Fei, L., 2009. Imagenet: A large-scale hierarchical image database, in: 2009 IEEE conference on computer vision and pattern recognition, Ieee. pp. 248–255.
- Donahue, J., Jia, Y., Vinyals, O., Hoffman, J., Zhang, N., Tzeng, E., Darrell, T., 2014. Decaf: A deep convolutional

- activation feature for generic visual recognition, in: International conference on machine learning, pp. 647–655.
- Faust, K., Bala, S., van Ommeren, R., Portante, A., Al Qawahmed, R., Djuric, U., Diamandis, P., 2019. Intelligent feature engineering and ontological mapping of brain tumour histomorphologies by deep learning. *Nature Machine Intelligence* 1, 316–321.
- Faust, K., Xie, Q., Han, D., Goyle, K., Volynskaya, Z., Djuric, U., Diamandis, P., 2018. Visualizing histopathologic deep learning classification and anomaly detection using nonlinear feature space dimensionality reduction. *BMC bioinformatics* 19, 173.
- Fu, Y., Jung, A.W., Torne, R.V., Gonzalez, S., Vohringer, H., Jimenez-Linan, M., Moore, L., Gerstung, M., 2019. Pan-cancer computational histopathology reveals mutations, tumor composition and prognosis. *bioRxiv* , 813543.
- Glorot, X., Bengio, Y., 2010. Understanding the difficulty of training deep feedforward neural networks, in: Proceedings of the thirteenth international conference on artificial intelligence and statistics, pp. 249–256.
- Gurcan, M.N., Boucheron, L., Can, A., Madabhushi, A., Rajpoot, N., Yener, B., 2009. Histopathological image analysis: A review. *IEEE reviews in biomedical engineering* 2, 147.
- Gutman, D.A., Cobb, J., Somanna, D., Park, Y., Wang, F., Kurc, T., Saltz, J.H., Brat, D.J., Cooper, L.A., Kong, J., 2013. Cancer digital slide archive: an informatics resource to support integrated *in silico* analysis of tcga pathology data. *Journal of the American Medical Informatics Association* 20, 1091–1098.
- Huang, G., Liu, Z., Van Der Maaten, L., Weinberger, K.Q., 2017. Densely connected convolutional networks, in: Proceedings of the IEEE conference on computer vision and pattern recognition, pp. 4700–4708.
- Janowczyk, A., Madabhushi, A., 2016. Deep learning for digital pathology image analysis: A comprehensive tutorial with selected use cases. *Journal of pathology informatics* 7.
- Jegou, H., Perronnin, F., Douze, M., Sánchez, J., Perez, P., Schmid, C., 2011. Aggregating local image descriptors into compact codes. *IEEE transactions on pattern analysis and machine intelligence* 34, 1704–1716.
- Kalra, S., Choi, C., Shah, S., Pantanowitz, L., Tizhoosh, H., 2019a. Yottixel—an image search engine for large archives of histopathology whole slide images. *arXiv preprint arXiv:1911.08748* .
- Kalra, S., Tizhoosh, H., Shah, S., Choi, C., Damaskinos, S., Safarpoor, A., Shafiei, S., Babaie, M., Diamandis, P., Campbell, C.J., et al., 2019b. Pan-cancer diagnostic consensus through searching archival histopathology images using artificial intelligence. *arXiv preprint arXiv:1911.08736* .
- Kather, J.N., Weis, C.A., Bianconi, F., Melchers, S.M., Schad, L.R., Gaiser, T., Marx, A., Zöllner, F.G., 2016. Multi-class texture analysis in colorectal cancer histology. *Scientific reports* 6, 27988.
- Kieffer, B., Babaie, M., Kalra, S., Tizhoosh, H.R., 2017. Convolutional neural networks for histopathology image classification: Training vs. using pre-trained networks, in: 2017 Seventh International Conference on Image Processing Theory, Tools and Applications (IPTA), IEEE. pp. 1–6.
- Kingma, D.P., Ba, J., 2014. Adam: A method for stochastic optimization. *arXiv preprint arXiv:1412.6980* .
- Kraus, O.Z., Grys, B.T., Ba, J., Chong, Y., Frey, B.J., Boone, C., Andrews, B.J., 2017. Automated analysis of high-content microscopy data with deep learning. *Molecular systems biology* 13.
- Kumar, M.D., Babaie, M., Tizhoosh, H.R., 2018. Deep barcodes for fast retrieval of histopathology scans, in: 2018 International Joint Conference on Neural Networks (IJCNN), pp. 1–8. doi:10.1109/IJCNN.2018.8489574.
- Kumar, M.D., Babaie, M., Zhu, S., Kalra, S., Tizhoosh, H.R., 2017. A comparative study of cnn, bovw and lbp for classification of histopathological images, in: 2017 IEEE Symposium Series on Computational Intelligence (SSCI), IEEE. pp. 1–7.
- Lee, H.S., Jung, H., Agarwal, A.A., Kim, J., 2017. Can deep neural networks match the related objects?: A survey on imagenet-trained classification models. *arXiv preprint arXiv:1709.03806* .
- Liu, L., Ouyang, W., Wang, X., Fieguth, P., Chen, J., Liu, X., Pietikäinen, M., 2018. Deep learning for generic object detection: A survey. *arXiv preprint arXiv:1809.02165* .
- Liu, Y., Gadepalli, K., Norouzi, M., Dahl, G.E., Kohlberger, T., Boyko, A., Venugopalan, S., Timofeev, A., Nelson, P.Q., Corrado, G.S., et al., 2017. Detecting cancer metastases on gigapixel pathology images. *arXiv preprint arXiv:1703.02442* .
- Madabhushi, A., 2009. Digital pathology image analysis: opportunities and challenges. *Imaging in medicine* 1, 7.
- Mormont, R., Geurts, P., Marée, R., 2018. Comparison of deep transfer learning strategies for digital pathology, in: Proceedings of the IEEE Conference on Computer Vision and Pattern Recognition Workshops, pp. 2262–2271.
- Najafabadi, M.M., Villanustre, F., Khoshgoftaar, T.M., Seliya, N., Wald, R., Muharemagic, E., 2015. Deep learning applications and challenges in big data analytics. *Journal of Big Data* 2, 1.
- Nanni, L., Ghidoni, S., Brahma, S., 2018. Ensemble of convolutional neural networks for bioimage classification. *Applied Computing and Informatics* .
- Niazi, M.K.K., Parwani, A.V., Gurcan, M.N., 2019. Digital pathology and artificial intelligence. *The Lancet Oncology* 20, e253–e261.
- Onder, D., Zengin, S., Sarioglu, S., 2014. A review on color normalization and color deconvolution methods in histopathology. *Applied Immunohistochemistry & Molecular Morphology* 22, 713–719.
- Phan, H.T.H., Kumar, A., Kim, J., Feng, D., 2016. Transfer learning of a convolutional neural network for hep-2 cell image classification, in: 2016 IEEE 13th International Symposium on Biomedical Imaging (ISBI), IEEE. pp. 1208–1211.
- Raghu, M., Zhang, C., Kleinberg, J., Bengio, S., 2019. Transfusion: Understanding transfer learning for medical imaging, in: Advances in Neural Information Processing Systems, pp. 3342–3352.
- Rajpurkar, P., Irvin, J., Zhu, K., Yang, B., Mehta, H., Duan,

- T., Ding, D., Bagul, A., Langlotz, C., Shpanskaya, K., et al., 2017. Chexnet: Radiologist-level pneumonia detection on chest x-rays with deep learning. arXiv preprint arXiv:1711.05225 .
- Sharif Razavian, A., Azizpour, H., Sullivan, J., Carlsson, S., 2014. Cnn features off-the-shelf: an astounding baseline for recognition, in: Proceedings of the IEEE conference on computer vision and pattern recognition workshops, pp. 806–813.
- Shin, H.C., Roth, H.R., Gao, M., Lu, L., Xu, Z., Nogues, I., Yao, J., Mollura, D., Summers, R.M., 2016. Deep convolutional neural networks for computer-aided detection: Cnn architectures, dataset characteristics and transfer learning. *IEEE transactions on medical imaging* 35, 1285–1298.
- Spanhol, F.A., Oliveira, L.S., Cavalin, P.R., Petitjean, C., Heutte, L., 2017. Deep features for breast cancer histopathological image classification, in: 2017 IEEE International Conference on Systems, Man, and Cybernetics (SMC), pp. 1868–1873. doi:10.1109/SMC.2017.8122889.
- Srivastava, R.K., Greff, K., Schmidhuber, J., 2015. Training very deep networks, in: Advances in neural information processing systems, pp. 2377–2385.
- Sun, H., Zeng, X., Xu, T., Peng, G., Ma, Y., 2019. Computer-aided diagnosis in histopathological images of the endometrium using a convolutional neural network and attention mechanisms. *IEEE Journal of Biomedical and Health Informatics* , 1–1doi:10.1109/JBHI.2019.2944977.
- Tizhoosh, H.R., Pantanowitz, L., 2018. Artificial intelligence and digital pathology: Challenges and opportunities. *Journal of pathology informatics* 9.
- Tizhoosh, H.R., Zhu, S., Lo, H., Chaudhari, V., Mehdi, T., 2016. Minmax radon barcodes for medical image retrieval, in: International Symposium on Visual Computing, Springer, pp. 617–627.
- Tomczak, K., Czerwińska, P., Wiznerowicz, M., 2015. The cancer genome atlas (tcga): an immeasurable source of knowledge. *Contemporary oncology* 19, A68.
- Travis, W.D., 2014. Pathology and diagnosis of neuroendocrine tumors: lung neuroendocrine. *Thoracic surgery clinics* 24, 257–266.
- Watanabe, S., Hori, T., Le Roux, J., Hershey, J.R., 2017. Student-teacher network learning with enhanced features, in: 2017 IEEE International Conference on Acoustics, Speech and Signal Processing (ICASSP), IEEE. pp. 5275–5279.
- Wei, J.W., Tafe, L.J., Linnik, Y.A., Vaickus, L.J., Tomita, N., Hassanpour, S., 2019. Pathologist-level classification of histologic patterns on resected lung adenocarcinoma slides with deep neural networks. *Scientific reports* 9, 3358.
- Yu, D., Deng, L., Seide, F.T.B., Li, G., 2016. Discriminative pretraining of deep neural networks. US Patent 9,235,799.
- Zhang, J., Lu, C., Li, X., Kim, H.J., Wang, J., 2019a. A full convolutional network based on densenet for remote sensing scene classification. *Math. Biosci. Eng* 16, 3345–3367.
- Zhang, K., Guo, Y., Wang, X., Yuan, J., Ding, Q., 2019b. Multiple feature reweight densenet for image classification. *IEEE Access* 7, 9872–9880.
- Zhu, S., Li, Y., Kalra, S., Tizhoosh, H.R., 2018. Multiple disjoint dictionaries for representation of histopathology images. *Journal of Visual Communication and Image Representation* 55, 243–252.

VI. APPENDIX

Code	Primary Diagnosis	#Patients
ACC	Adrenocortical Carcinoma	86
BLCA	Bladder Urothelial Carcinoma	410
BRCA	Breast Invasive Carcinoma	1097
CESC	Cervical Squamous Cell Carcinoma and Endocervical Adenoc.	304
CHOL	Cholangiocarcinoma	51
COAD	Colon Adenocarcinoma	459
DLBC	Lymphoid Neoplasm Diffuse Large B-cell Lymphoma	48
ESCA	Esophageal Carcinoma	185
GBM	Glioblastoma Multiforme	604
HNSC	Head and Neck Squamous Cell Carcinoma	473
KICH	Kidney Chromophobe	112
KIRC	Kidney Renal Clear Cell Carcinoma	537
KIRP	Kidney Renal Papillary Cell Carcinoma	290
LGG	Brain Lower Grade Glioma	513
LIHC	Liver Hepatocellular Carcinoma	376
LUAD	Lung Adenocarcinoma	522
LUSC	Lung Squamous Cell Carcinoma	504
MESO	Mesothelioma	86
OV	Ovarian Serous Cystadenocarcinoma	590
PAAD	Pancreatic Adenocarcinoma	185
PCPG	Pheochromocytoma and Paraganglioma	179
PRAD	Prostate Adenocarcinoma	499
READ	Rectum Adenocarcinoma	170
SARC	Sarcoma	261
SKCM	Skin Cutaneous Melanoma	469
STAD	Stomach Adenocarcinoma	442
TGCT	Testicular Germ Cell Tumors	150
THCA	Thyroid Carcinoma	507
THYM	Thymoma	124
UCEC	Uterine Corpus Endometrial Carcinoma	558
UCS	Uterine Carcinosarcoma	57
UVM	Uveal Melanoma	80

TABLE VI
THE TCGA CODES (IN ALPHABETICAL ORDER) OF ALL 32 PRIMARY DIAGNOSES AND CORRESPONDING NUMBER OF EVIDENTLY DIAGNOSED PATIENTS IN THE DATASET (TCGA = THE CANCER GENOME ATLAS)